

# Redox-Active AIEgen-Derived Plasmonic and Fluorescent Core@Shell Nanoparticles for Multimodality Bioimaging

Xuewen He,<sup>†,‡,§</sup> Zheng Zhao,<sup>†,‡</sup> Ling-Hong Xiong,<sup>†,‡,§</sup> Peng Fei Gao,<sup>†,‡,||</sup> Chen Peng,<sup>†,‡,#</sup> Rong Sheng Li,<sup>||</sup> Yu Xiong,<sup>†,‡</sup> Zhi Li,<sup>¶</sup> Herman H.-Y. Sung,<sup>†</sup> Ian D. Williams,<sup>†</sup> Ryan T. K. Kwok,<sup>†,‡,§</sup> Jacky W. Y. Lam,<sup>†,‡</sup> Cheng Zhi Huang,<sup>||,¶</sup> Nan Ma,<sup>¶</sup> and Ben Zhong Tang<sup>\*,†,‡,§,□,||,¶</sup>

<sup>†</sup>Department of Chemistry, Hong Kong Branch of Chinese National Engineering Research Centre for Tissue Restoration and Reconstruction, Institute for Advanced Study, Division of Life Science, and Division of Biomedical Engineering, The Hong Kong University of Science and Technology, Clear Water Bay, Kowloon, Hong Kong

<sup>‡</sup>HKUST-Shenzhen Research Institute, Shenzhen, 518057, China

<sup>§</sup>Shenzhen Center for Disease Control and Prevention, Shenzhen, 518055, China

<sup>||</sup>Key Laboratory of Luminescent and Real-Time Analytical Chemistry (Southwest University), Ministry of Education, College of Pharmaceutical Sciences, Southwest University, Chongqing, 400716, China

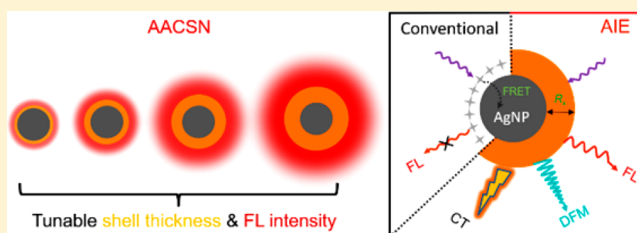
<sup>#</sup>Department of Radiology, Shanghai Tenth People's Hospital, School of Medicine, Tongji University, Shanghai, 200072, China

<sup>¶</sup>The Key Lab of Health Chemistry and Molecular Diagnosis of Suzhou, College of Chemistry, Chemical Engineering and Materials Science, Soochow University, Suzhou, 215123, China

<sup>□</sup>NSFC Center for Luminescence from Molecular Aggregates, SCUT-HKUST Joint Research Laboratory, State Key Laboratory of Luminescent Materials and Devices, South China University of Technology, Guangzhou, 510640, China

## Supporting Information

**ABSTRACT:** Multimodality imaging is highly desirable for accurate diagnosis by achieving high sensitivity, spatial–temporal resolution, and penetration depth with a single structural unit. However, it is still challenging to integrate fluorescent and plasmonic modalities into a single structure, as they are naturally incompatible because of significant fluorescence quenching by plasmonic noble-metal nanoparticles. Herein, we report a new type of silver@AIEgen (aggregation-induced emission luminogen) core–shell nanoparticle (AACSN) with both strong aggregated-state fluorescence of the AIEgen and distinctive plasmonic scattering of silver nanoparticles for multimodality imaging in living cells and small animals. The AACSNs were prepared through a redox reaction between silver ions and a redox-active AIEgen, which promoted synergistic formation of the silver core and self-assembly of the AIEgen around the core. The resulting AACSNs exhibited good biocompatibility and high resistance to environmental damage. As a result, excellent performance in fluorescence imaging, dark-field microscopy, and X-ray computed tomography-based multimodality imaging was achieved.



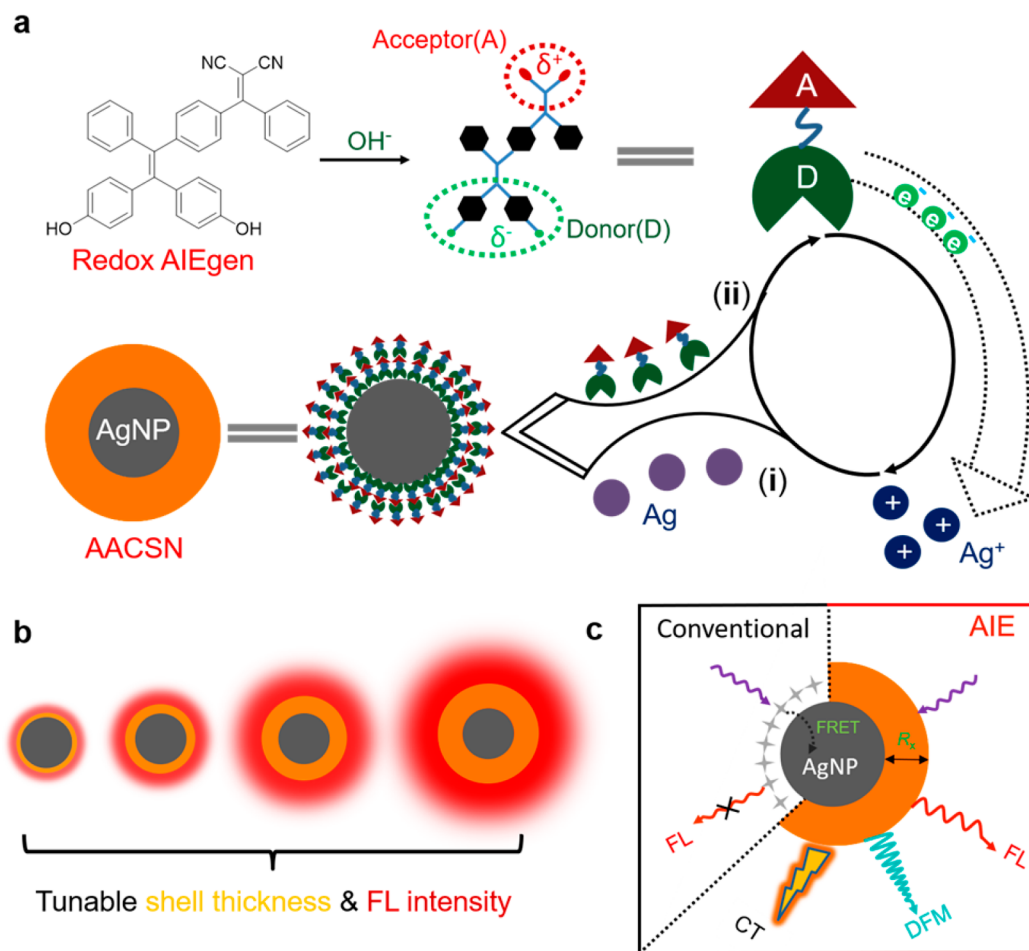
## INTRODUCTION

Biological detection and clinical diagnostics propel the development of advanced technologies for subcellular, cellular, and tissue imaging.<sup>1,2</sup> To this end, various types of bioimaging probes have been developed with high sensitivity, spatial–temporal resolution, and excellent depth penetrability.<sup>3,4</sup> Fluorescence (FL) imaging is an essential tool for *in situ* visualization of bioanalytes at the molecular level and monitoring complex biological processes in real time.<sup>5</sup> The red to near-infrared fluorescence could offer minimized autofluorescence interference in living systems.<sup>6</sup> However, the performance of most fluorophores is still limited by the photobleaching effect and moderate signal-to-noise ratio, and their applicability for *in vivo* imaging is restricted to a superficial region.<sup>7,8</sup> Although inorganic nanoparticles such as quantum dots or upconverting nanoparticles possess bright fluorescence and

good photostability,<sup>9–12</sup> their heavy metal components would cause further toxicity concerns.<sup>13,14</sup> To obtain complementary information for the fluorescence imaging modality, it is ideal to integrate other imaging modalities with high signal-to-noise ratio, high spatial resolution, and deep tissue penetration capability in a single probe. For example, the localized surface plasmonic resonance (LSPR) of the noble metal has been applied to dark-field microscopy (DFM) imaging with high signal-to-noise ratio.<sup>15–17</sup> The extremely large scattering cross-section of DFM prevents interference of the ensemble averaging effect for optical scattering imaging and single-nanoparticle analysis.<sup>18</sup> Also, noble-metal nanoparticle-based computed tomography (CT)

Received: February 28, 2018

Published: May 9, 2018

Scheme 1. Schematic Illustrations of the Synthesis, Tunable Properties, and Multimodality Imaging Application of AACSN<sup>a</sup>

<sup>a</sup>The redox AIEgen possessed an electron donor–acceptor (D–A) structure. (a) The synthesis of AACSN included (i) a reduction reaction and (ii) an AIEgen self-assembly process. (b) The obtained AACSN had a tunable shell thickness and fluorescence properties. (c) Integration of fluorescent and plasmonic moieties for multimodality imaging. In a conventional fluorophore’s system, the fluorescence was quenched via a FRET or ET process, while in an AIE system, these two moieties coexisted with tunable shell thickness ( $R_x$ ). As a result, the AACSN could be applied in FL, DFM, and CT multimodality imaging.

could offer high spatial resolution, 3D tomography information, and deep tissue penetration capability for *in vivo* imaging.<sup>19,20</sup> However, direct combination of fluorophores and noble metals in a single nanostructure would cause severe loss of fluorescence signals due to quenching effects of the plasmonically active noble-metal nanoparticle via fluorescence resonance energy transfer (FRET) or electronic transfer (ET).<sup>21–24</sup> Spatial separation of these two components in multilayered nanostructures is possible, yet the ensemble fluorescence intensity is compromised by the self-quenching effect at high local fluorophore concentration as well as their limited photostability.<sup>25–27</sup>

Unlike conventional organic fluorophores, luminogens with aggregation-induced emission (AIEgens)<sup>28</sup> with propeller-shaped structures provide a superior choice for light-up fluorescence imaging.<sup>29–32</sup> As isolated molecules, the rotor-containing AIEgens undergo low-frequency motions and dissipate exciton energy, leading to fast nonradiative decay of the excited states and weak emission. In the aggregated form, the radiative pathway is predominant for strong emission via the restriction of intramolecular rotation, vibration, and motion.<sup>8,33</sup> The AIEgen aggregates exhibit large absorptivity, robust luminosity, strong photobleaching resistance, no random blinking, and excellent

biocompatibility.<sup>34,35</sup> They have been widely applied for *in vitro* and *in vivo* bioimaging, including specific biomolecular analysis,<sup>36,37</sup> real-time organelle or cellular imaging,<sup>38–40</sup> long-lasting drug delivery tracking,<sup>41</sup> and high-resolution cerebral vessel visualization.<sup>42,43</sup> Aggregation of AIEgens could be induced by enzymatic catalysis,<sup>44</sup> chemical reaction,<sup>45,46</sup> environmental response,<sup>47</sup> etc. However, reduction of metal ion-induced AIEgen aggregation and synergistic formation of metal@AIEgen core-shell nanostructures have not been previously demonstrated.

Herein, we report the preparation of a new class of plasmonic fluorescent silver@AIEgen core-shell nanoparticles (AACSNs) for multimodality imaging. AACSNs were fabricated via a redox reaction between the phenolic hydroxyl group of an AIEgen and silver ions ( $\text{Ag}^+$ ). The formation of silver nanoparticles (AgNPs) simultaneously induced aggregation of AIEgens around the AgNP to form core-shell hybrid nanostructures (Scheme 1). The electron donor–acceptor (D–A) structure of AIEgens guided their intermolecular self-assembly to form the organic shell layer with tunable shell thickness and fluorescence intensity under various AIEgen concentrations. This facile strategy overcame the challenges of integrating fluorescent and plasmonic modalities into a single probe with preserved properties.

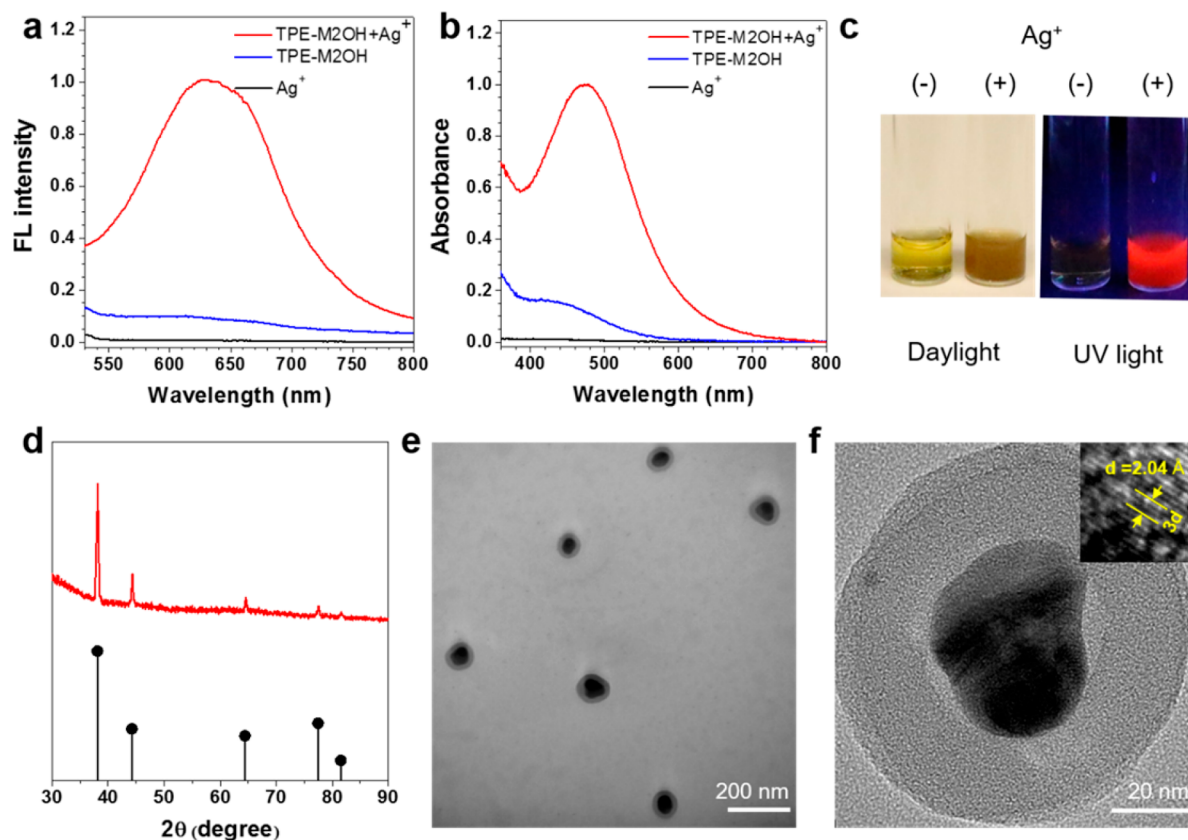


**Figure 1.** Characterization of AACSNs. (a) FL spectra and (b) absorption spectra of TPE-M2OH with or without adding  $\text{Ag}^+$  and  $\text{Ag}^+$  alone under pH 10.5 condition. (c) Digital photos of an AIEgen solution under ambient light (left) and 365 nm UV light (right) with or without  $\text{Ag}^+$ . (d) XRD spectrum of AACSN and standard JCPDS pattern (04-0783) of the silver crystallite. (e) TEM and (f) high-resolution TEM images of the AACSNs. Inset indicates crystallite pattern of the core with a lattice spacing of 2.04 Å.

The AACSN was successfully demonstrated with FL, DFM, and CT imaging.

## RESULTS AND DISCUSSION

### Synthesis, Characterization, and Properties of AACSNs.

AACSNs were prepared via a redox reaction and subsequent self-assembly process using a phenol-group-containing redox AIEgen (TPE-M2OH) and  $\text{Ag}^+$  as precursors (Scheme 1). Synthesis and characterization of TPE-M2OH were detailed in the Supporting Information (SI) (Figure S1). TPE-M2OH exhibited an apparent AIE property. No fluorescence was emitted when it was dissolved in a good solvent, tetrahydrofuran (THF), whereas strong aggregated-state emission with 9.3 times enhancement in intensity appeared in water (Figure S2). Co-incubation of  $\text{Ag}^+$  and TPE-M2OH in alkaline solution (pH 10.5) led to quick darkening of the solution color, indicating the occurrence of a redox reaction. As shown in Figure 1a, compared to TPE-M2OH, the reaction product exhibited significantly enhanced fluorescence with an emission maximum at 640 nm, indicating the formation of TPE-M2OH aggregates. In addition, an obvious increase of absorbance appeared in the range between 400 and 500 nm with a maximum at 485 nm, which corresponded to the characteristic absorption of AgNP (Figure 1b). Changes in solution color and fluorescence intensity could be directly visualized in photographs of the reaction mixture taken under ambient light and 365 nm UV light (Figure 1c). Powder X-ray diffraction (XRD) analysis revealed formation of a silver crystallite that matched with the standard JCPDS pattern (No. 04-0783) (Figure 1d). Transmission

electron microscopy (TEM) images showed the production of a uniform near-monodisperse core–shell structure with a mean diameter of about 85 nm (Figure 1e and Figure S5). A high-resolution TEM image of a single particle showed that the diameter of the AgNP core was about 45 nm and the AIEgen shell thickness was about 20 nm. The lattice spacing (ca. 2.04 Å) of the core matched well with the distance of the adjacent facet (200) of the silver crystallite, which corresponded to the peak at  $2\theta = 44.3^\circ$  in the XRD pattern (inset of Figure 1f). The amorphous layer around the core with light contrast could be attributed to the as-formed organic AIEgen aggregate.

The shell thickness and fluorescence properties of AACSN were tunable using various concentrations of the AIEgen for the reaction. The as-prepared AACSN was purified via centrifugation before characterization (Figure S6). As shown in Figure 2a, the fluorescence of the AACSN was steadily enhanced by increasing the TPE-M2OH concentration from 50  $\mu\text{M}$  to 625  $\mu\text{M}$  (Figure 2c). Meanwhile, an increased concentration of TPE-M2OH led to a higher concentration of AgNPs, as revealed by the absorption spectra (Figure 2b). TEM images showed that near-spherical AACSNs were produced under all the tested conditions (Figure 2d and Figure S7). The shell thickness increased from 16.9 nm to 29.8 nm as the concentration of TPE-M2OH increased from 125 to 500  $\mu\text{M}$  (Figure 2c). The hydrodynamic size of the AACSNs via dynamic light scattering (DLS) measurements also presented an increasing trend (Figure S8). In addition, the reaction time and temperature played important roles in tuning the shell thickness (Figures S9–S12). The Förster distance between the AgNP

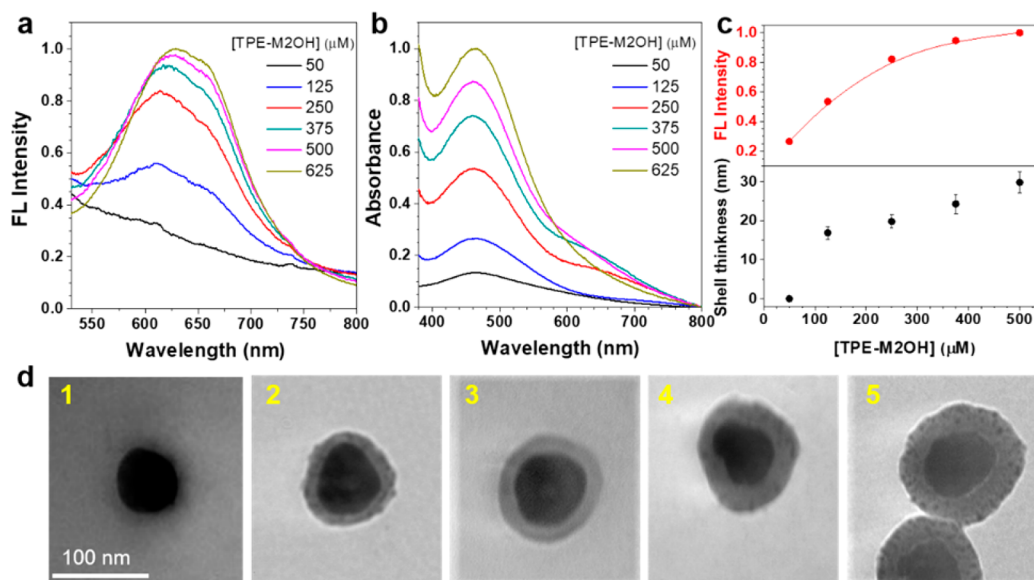


**Figure 2.** Tuning the shell thickness of AACSNs. (a) FL spectra and (b) absorption spectra of obtained AACSNs under different concentrations of TPE-M2OH. (c) Dependence of shell thicknesses and FL intensities at 640 nm on TPE-M2OH concentrations. (d) Representative TEM images of AACSNs produced by 50, 125, 250, 375, and 500  $\mu\text{M}$  TPE-M2OH from 1 to 5, respectively. Their corresponding statistic shell thicknesses were 0 nm (without obvious shell),  $16.9 \pm 1.68$  nm ( $n = 248$ ),  $19.8 \pm 1.75$  nm ( $n = 230$ ),  $24.3 \pm 2.49$  nm ( $n = 252$ ), and  $29.8 \pm 2.75$  nm ( $n = 214$ ), respectively. “ $n$ ” is the number of nanoparticles in the TEM images for statistic calculation.

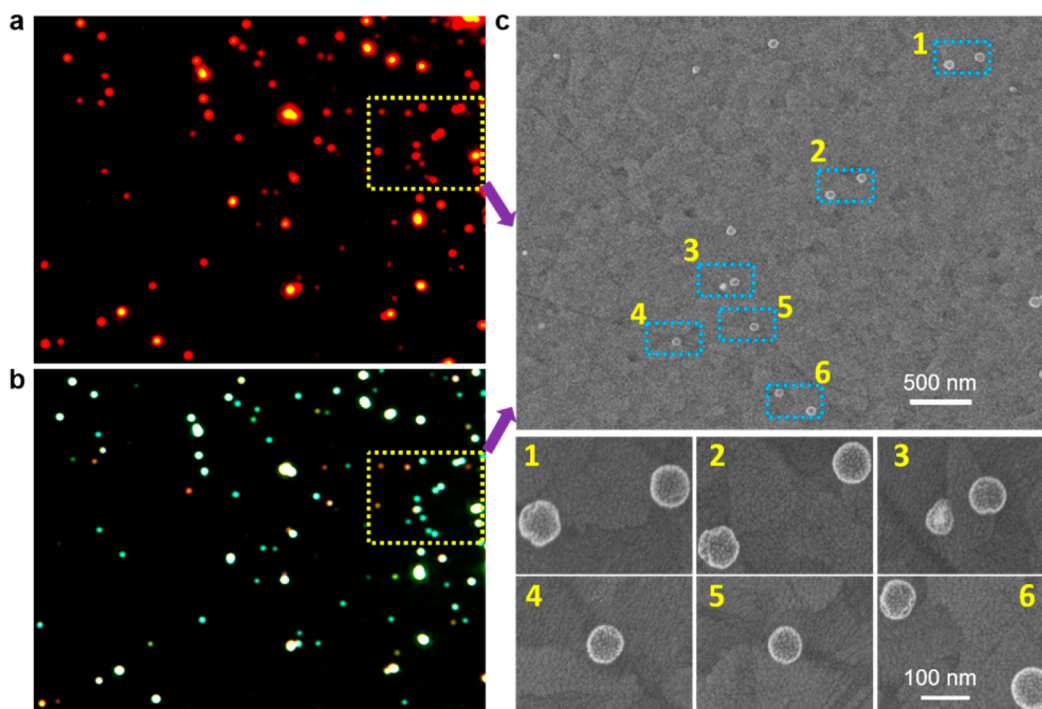


**Figure 3.** Single-nanoparticle analysis of AACSNs ( $\sim 20$  nm shell thickness). (a) FL image of AACSNs. (b) DFM image of AACSNs of the same region. (c) SEM image of AACSNs in the yellow box area in FL and DFM images and high-amplification images of each numbered area. The FL and DFM imaging were obtained under a  $100\times$  oil objective.

core and the AIE shell was calculated to be 6.89 nm (Figure S13). Therefore, strong emission of the AACSN could be achieved when the shell thickness exceeded the Förster distance.

We subsequently investigated the performance of AACSN for DFM imaging. In single-particle microscopy, the fluorescence signal (red) and scattering signal (cyan) were observed as numerous isolated spots (Figure 3a,b). The perfect overlapping of fluorescence and DFM signals suggested that the two signals

originated from the same particles (Figure S14). Particles in the selected area in fluorescence and DFM images were further characterized with scanning electron microscopy (SEM). Each spot was identified as a single particle, confirming that the fluorescence and DFM signals originated from individual particles (Figure 3c and Figure S14).

We next evaluated the stability of the AACSNs under an oxidative environment by monitoring the DFM signal over the

incubation time (Figure S15). As a control, the DFM signal of sodium citrate-capped AgNPs dimmed continuously with a more than 50% intensity decrease after 3 h. In contrast, the signal of the AACSNs remained almost unchanged during the same period. This enhanced stability against oxidization could be attributed to the protective shell formed by self-assembly of AIEgen molecules on AgNPs.

The dependence of TPE-M2OH aggregation on  $\text{Ag}^+$  concentration was further investigated. In the absence of  $\text{Ag}^+$  in alkaline buffer, no absorption or fluorescence change was observed for TPE-M2OH (Figure 1a,b). However, when the  $\text{Ag}^+$  concentration increased from 0  $\mu\text{M}$  to 1500  $\mu\text{M}$ , the fluorescence intensity of the mixture gradually increased to a maximum at 200  $\mu\text{M}$  of  $\text{Ag}^+$  and then dropped at higher  $\text{Ag}^+$  concentrations (Figure S16). These results suggested that the  $\text{Ag}^+$  played a crucial role in inducing shell formation and AIE fluorescence. The fluorescence intensity was expected to be dependent on the AIE shell thickness and the concentration of formed AACSNs. The continuous increase in absorbance suggested that more AgNPs were produced with increasing  $\text{Ag}^+$  concentration. The TEM images showed that the shell thickness of AACSNs generated at 1000  $\mu\text{M}$   $\text{Ag}^+$  was much thinner than that generated at 200  $\mu\text{M}$   $\text{Ag}^+$  (Figure S17), leading to lower fluorescence intensity at 1000  $\mu\text{M}$   $\text{Ag}^+$ . The formation of AACSNs was also highly dependent on pH (Figure S18). It had been previously reported that the phenol group possessed reducing capability in alkaline condition.<sup>48</sup> The mixture of  $\text{Ag}^+$  and TPE-M2OH under neutral pH presented no apparent color change (Figure S19). Because TPE-M2OH was insoluble, emissive TPE-M2OH aggregates were formed and even precipitated out when the molar ratio of  $\text{Ag}^+$  to TPE-M2OH surpassed 1.5. However, there was no core-shell structure formed in the TEM images (Figure S19d). Under elevated pH, the phenol group of TPE-M2OH was deprotonated, and thus TPE-M2OH became soluble in the aqueous medium, which resulted in the disappearance of FL signals at around pH 10.5 (Figure S20). The FL was recovered upon  $\text{Ag}^+$  addition (Figure S16) as a result of TPE-M2OH aggregation induced by reduction of  $\text{Ag}^+$  at elevated pH. In short, the redox capability of TPE-M2OH in alkaline condition determined the AgNP generation, which in turn induced the self-assembly of TPE-M2OH to form AACSNs.

#### Mechanistic Investigation of AIEgen Self-Assembly.

The roles of the molecular structure of TPE-M2OH in self-assembly were explored with two redox AIEgen analogues: TPE-N2OH and TPE-2OH (Figure S1). They also exhibited obvious AIE properties with 8.4 and 8.9 times enhancement in fluorescence intensity after aggregation in water, respectively (Figures S3 and S4). Like TPE-M2OH, both TPE-N2OH and TPE-2OH contained two phenol groups in their molecular structure acting as electron donors, whereas they were different in electron acceptor domains. Cyclic voltammetry (CV) measurements showed that the oxidation potentials of TPE-N2OH, TPE-2OH, and TPE-M2OH were located at 0.763, 0.952, and 1.234 V, respectively (Figure S21), indicating that all the molecules were redox-active with reducing capability in the order TPE-N2OH > TPE-2OH > TPE-M2OH. After incubation with  $\text{Ag}^+$  under alkaline condition, TPE-M2OH self-assembled into a shell layer with strong FL (Figure 1a,e), whereas TPE-N2OH and TPE-2OH did not form a shell layer and no emission was detected (Figure 4d,e,g,h and Figure S22). X-ray photoelectron spectroscopy data also suggested the binding of TPE-M2OH to the silver nanocore (Figure S23). The difference in the size of the AgNP

produced by the three AIEgens could be attributed to their different redox potentials, which were not the determinant factors for AIEgen self-assembly.

When the phenol group was deprotonated in alkaline condition, TPE-M2OH would form electron-rich and -poor domains that were located at opposite ends. Under the same conditions, TPE-N2OH and TPE-2OH formed two electron-rich ends and one electron-rich end, respectively (Figure 4a,c,f). Therefore, the self-assembly capability of TPE-M2OH should be closely related to its electron D-A structure. The density functional theory calculation of TPE-M2OH verified its typical D-A structure, in which the HOMO and LUMO were contributed by its electron-rich and electron-poor tail, respectively. However, the HOMO and LUMO orbitals of TPE-N2OH and TPE-2OH were not separated (Figure S24). The D-A structure of TPE-M2OH was further supported by its solvatochromic effect, leading to a gradual red-shift of the FL maximum with increasing solvent polarity (Figure S25). The single-crystal structure of TPE-M2OH (CCDC ref number 1817311) further confirmed the head-to-tail intermolecular arrangement pattern, formed by electrostatic interaction, hydrogen bonding, and intermolecular C-H $\cdots$  $\pi$  interactions (Figure S26).

**In Vitro and in Vivo Multimodality Imaging.** The colloidal stability and cytotoxicity of AACSNs were investigated before imaging studies. As shown in Figure S27, the absorbance and fluorescence intensity of AACSNs exhibited little change after 15-day storage. The hydrodynamic size distribution and average diameter after storage were similar to the freshly prepared samples (Figure S28). Tests in cell lysates and serum further indicated the good stability of AACSNs in a bioenvironment (Figures S29 and S30). The cytotoxicity assay showed that the HeLa cells maintained over 95% viability at a concentration of 100  $\mu\text{g}/\text{mL}$  AACSN (Figure S31). This concentration corresponded to 67.4  $\mu\text{g}/\text{mL}$  of AgNPs through ICP-AES measurement. The bare AgNPs synthesized by sodium citrate with a similar diameter caused  $\sim$ 50% cell death at a concentration of 15.0  $\mu\text{g}/\text{mL}$ . The improved biocompatibility of AACSN could be attributed to isolation of AgNPs by the AIEgen shell, which minimized their toxicity to living cells.<sup>49</sup>

Based on their unique optical properties, excellent stability, and biocompatibility, AACSNs were employed for *in vitro* and *in vivo* multimodality imaging. For fluorescence imaging, AACSNs were incubated with HeLa cells for 2 h at 37  $^{\circ}\text{C}$ . AACSNs could be readily internalized into HeLa cells and emit strong FL in the cells in a concentration-dependent manner (Figure S32). A high FL enhancement factor of 25 was achieved at 7.5  $\mu\text{g}/\text{mL}$  AACSN. The intracellular localization of AACSNs was studied by colocalization with LysoTracker Green DND-26, a marker for late endosomes and lysosomes. The high degree of overlapping of green and red color fluorescence with a Pearson's colocalization coefficient of 0.89 suggested that the AACSNs were internalized into endosomes and lysosomes (Figure S33). The fluorescence and DFM dual-modality imaging of living cells with AACSNs was then performed. As shown in Figure 5a,b, HeLa cells incubated with AACSNs ( $\sim$ 20 nm shell thickness) exhibited both strong fluorescence and DFM signals in the cells. Punctate patterns of DFM signals could be clearly visualized in high-magnification cell images. When AACSNs with reduced shell thickness (24 to 17 nm) were applied to cell imaging, the DFM signal exhibited negligible change, whereas the fluorescence signal decreased (Figure S34). HeLa cells incubated with TPE-M2OH alone also exhibited fluorescence signals due to formation of intracellular aggregation.

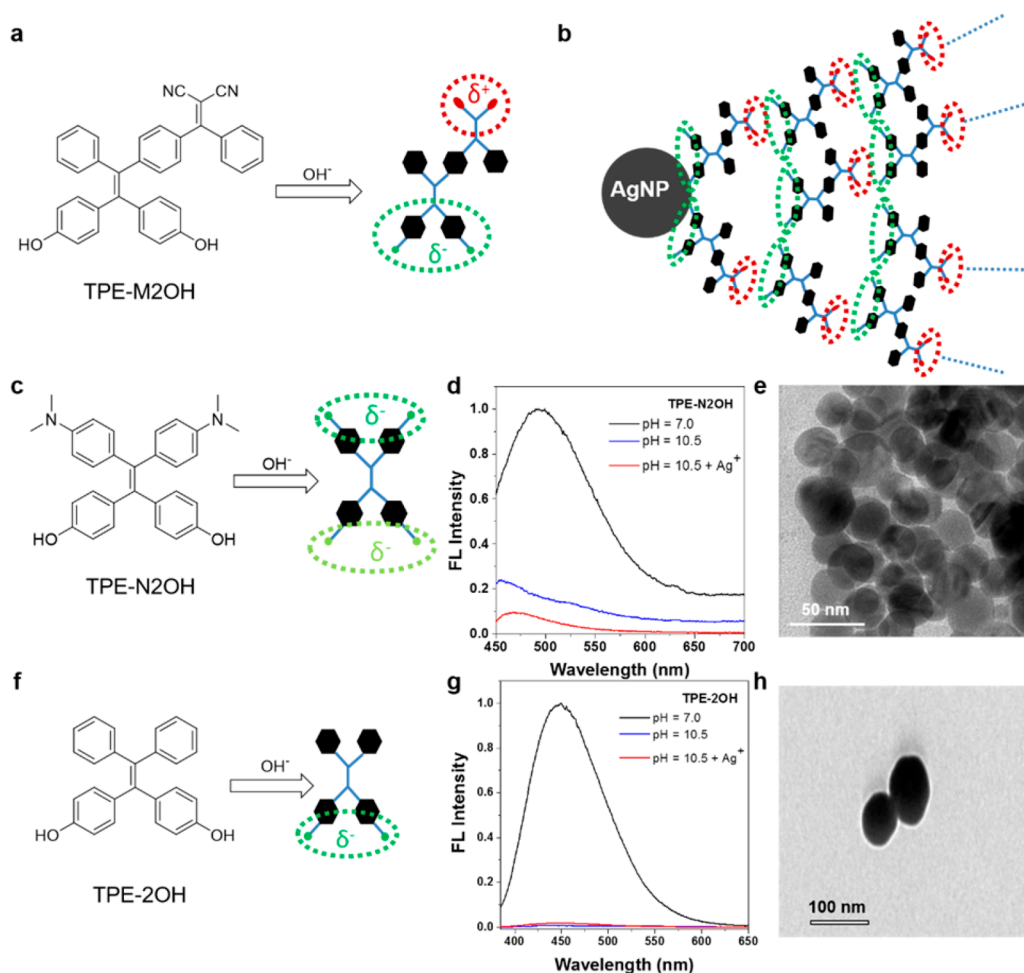


**Figure 4.** Self-assembly mechanism of AIEgens on the surface of AgNPs. Schematics of the electron-rich and -poor domains of (a) TPE-M2OH, (c) TPE-N2OH, and (f) TPE-2OH under alkaline condition. (b) Schematics of the presumed self-assembly mechanism of TPE-M2OH on the surface of AgNPs via the attraction between its electron-rich and -poor domains. FL spectra of AgNPs synthesized by (d) TPE-N2OH and (g) TPE-2OH. TEM images of AgNPs synthesized by (e) TPE-N2OH and (h) TPE-2OH.

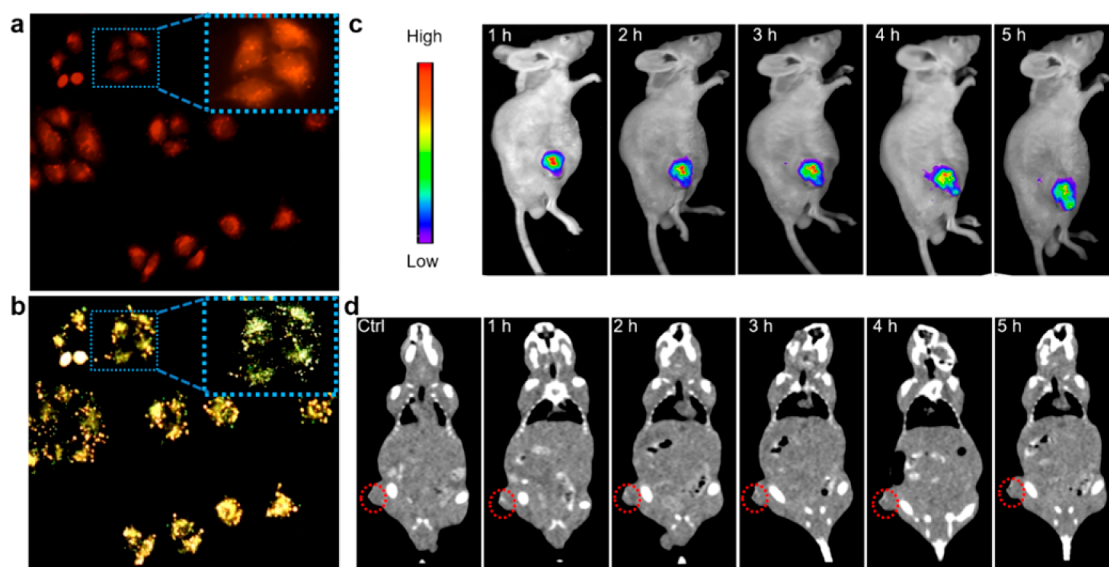


**Figure 5.** AACSNs for *in vitro* and *in vivo* multimodality imaging. The shell thickness of the AACSNs was  $\sim 20$  nm. (a) FL image of HeLa cells. It was obtained with a 20 $\times$  objective, and the inset picture with amplified selected area was obtained with a 63 $\times$  objective. (b) DFM image of the same region with the same amplification. (c) FL images and (d) CT images of 4T1 tumor-bearing nude mice at different time points after intratumoral injection of AACSNs. The tumor site is highlighted with a red dotted circle.

However, no characteristic DFM signals were detected due to the lack of a AgNP core (Figure S35).

To investigate the X-ray attenuation effects of AACSN probes (~20 nm shell thickness), CT imaging was performed under a wide AACSN concentration range. As shown in Figure S36, X-ray attenuation of AACSNs possessed a linear relationship with agent concentrations. The CT signal enhancement of the AACSNs was up to 408 HU at 20 mg/mL concentration, which was comparable to the clinical iodinated CT contrast agent at the same concentration.<sup>50</sup> Next, we applied AACSNs for fluorescence and CT dual-modality imaging in living mice. BALB/c-nude mice were intratumorally injected with AACSNs at a dosage of 50  $\mu$ L (25 mg/mL), followed by fluorescence and CT imaging at different time intervals. The fluorescence and CT images both displayed clear signal enhancements in tumor site in comparison with the surrounding tissue and the preinjection control (Figure 5c,d). The CT signal enhancement for post injection images was up to 183 HU after 5 h of tracking in CT modality (Figure S37). Intraperitoneal (i.p.) injection showed accumulation of AACSNs at the tumor site (Figure S38). Tumor accumulation of AACSNs reached a maximum after ~2 h and then gradually cleared from the tumor site after 10 h (Figure S39). Further *in vivo* toxicity assessment (Figures S40 and S41) suggested that AACSNs could offer good biosafety for *in vivo* imaging.

## CONCLUSIONS

In conclusion, we reported a new class of AgNP@AIEgen core-shell nanoparticles for multimodality imaging in living cells and animals. In addition to the excellent fluorescence property of the AIEgen shell, DFM and CT imaging modalities were successfully integrated into the probe via a AgNP core. The reported strategy resolved the challenges of integrating fluorescent and plasmonic materials in a single structure with preserved properties. The AACSNs exhibited high biocompatibility and colloidal stability to oxidative environments because of AIEgen shelling. The superior AIE fluorescence together with the high signal-to-noise ratio of DFM and the deep penetration depth of CT modalities offer great promise for advanced diagnostic applications.

## EXPERIMENTAL SECTION

The materials are listed in Section A in the SI. Synthetic routes of AIEgens, including 2-[[4-[2,2-bis(4-hydroxyphenyl)-1-phenylvinyl]-phenyl]methylene]malononitrile (TPE-M2OH), 4,4'-[2,2-bis[4-(diethylamino)phenyl]ethene-1,1-diyl]diphenol (TPE-N2OH), and 4,4'-[2,2-diphenylethene-1,1-diyl]diphenol (TPE-2OH) are described in Section B in the SI referring to previous report<sup>51</sup> with modifications. The AIE property of each AIEgen was demonstrated by studying their AIE fluorescence behaviors in a mixture of THF and water with different volume ratios (Section C in the SI). Their structures were characterized by NMR and high-resolution mass spectroscopy (Section R in the SI).

**Synthesis of AACSN Nanoparticles.** Typically, the AACSNs with a 20 nm shell thickness were synthesized as follows: 10  $\mu$ L of TPE-M2OH (25 mM dissolved in DMSO) was added to Na<sub>2</sub>CO<sub>3</sub>-NaHCO<sub>3</sub> pH buffer (pH = 10.5). Then, 2.0  $\mu$ L of AgNO<sub>3</sub> (100 mM in water) was added. The total volume was adjusted to 1000  $\mu$ L. The mixture was gently shaken at room temperature for 8 h. Afterward, the product was centrifuged at 12 000 rpm for 3 min and repeated twice. The generated AACSNs were redispersed in water for subsequent experiments.

**Confocal Imaging of Living Cells.** HeLa cells ( $1.5 \times 10^5$  cells per well) were seeded into a six-well confocal plate (Corning). After 24 h of incubation, the cells were washed once with 1 $\times$  phosphate-buffered

saline (PBS). A 10  $\mu$ L amount of AACSNs (~20 nm shell thickness, 100  $\mu$ g/mL) was diluted in 200  $\mu$ L of Dulbecco's modified Eagle's medium (without serum) at room temperature. Then the cells were incubated for 2 h at 37  $^{\circ}$ C in a humidified incubator containing 5% CO<sub>2</sub>. After washing with 1 $\times$  PBS three times, the cells were incubated with LysoTracker Green (2.0  $\mu$ L, 1:1000 diluted in serum-free cell culture medium) for another 20 min. After washing three times, the fluorescence images were acquired on a Leica TCS SP5 II confocal laser scanning microscope using a 63 $\times$  oil immersion objective (AACSNs were excited at 450 nm, and their emission was collected at 600–700 nm; LysoTracker Green was excited at 476 nm, and its emission was collected at 500–560 nm).

**Dark-Field Imaging.** A 100 W halogen light source (U-LH100-3) was used for DFM imaging. The AACSNs or the cells were placed on glass slides, and the samples were imaged with a spectrograph (MicroSpec-2300i, Roper Scientific) and intensified charge coupled device (CCD) camera (PI-MAX, Princeton Instrument) connected to the BX51 dark-field optical microscope (Olympus, Japan) equipped with a DP72 single-chip true-color CCD camera.

**In Vivo CT and Fluorescence Imaging.** Male BALB/c nude mice (4 weeks of age) were obtained from Shanghai Slac Laboratory Animal Co., Ltd. Animal experiments were performed according to protocols approved by the ethical committee of Shanghai Tenth People's Hospital for animal care, and all handling of mice was also in accordance with the regulations of the National Ministry of Health. In the right flank regions of the mice,  $1.0 \times 10^6$  4T1 cells/mouse were subcutaneously injected to establish the 4T1 tumor model. The volume of tumors was allowed to reach ~200 mm<sup>3</sup> before the CT/fluorescence imaging. For *in vivo* imaging, the mice were intratumorally injected with AACSNs (~20 nm shell thickness, 25 mg/mL, 50  $\mu$ L per mouse). The mice were scanned before and after injection by a dual-source CT system (SOMATOM Definition Flash, Siemens, Erlangen, Germany) at 80 kV, 110 mA, and a slice thickness of 0.6 mm. The fluorescence imaging was acquired using a Bruker In-Vivo F PRO imaging system (Billerica, MA, USA). The excitation was 485 nm, and the signal collection was 600–700 nm.

## ASSOCIATED CONTENT

### Supporting Information

The Supporting Information is available free of charge on the ACS Publications website at DOI: 10.1021/jacs.8b02350.

Materials, methods, supporting figures (Section A–S and Figures S1–S41) (PDF)

Crystallographic information files (CIF)

## AUTHOR INFORMATION

### Corresponding Author

\*tangbenz@ust.hk

### ORCID

Xuwen He: 0000-0002-8414-5164

Ryan T. K. Kwok: 0000-0002-6866-3877

Cheng Zhi Huang: 0000-0002-1260-5934

Nan Ma: 0000-0001-6352-300X

Ben Zhong Tang: 0000-0002-0293-964X

### Notes

The authors declare no competing financial interest.

## ACKNOWLEDGMENTS

The authors acknowledge funding to B.Z.T. from the Innovation and Technology Commission (ITC-CNERC14SC01), The National Science Foundation of China (21788102), the National Basic Research Program of China (973 Program: 2013CB834701 and 2013CB834702), and the Research Grants Council of Hong Kong (16301614, 16305015, N\_HKUST604/14, and A-HKUST605/16). B.Z.T. is also grateful for the support

from the Science and Technology Plan of Shenzhen (JCYJ20160229205601482).

## REFERENCES

- (1) Etzioni, R.; Urban, N.; Ramsey, S.; McIntosh, M.; Schwartz, S.; Reid, B.; Radich, J.; Anderson, G.; Hartwell, L. *Nat. Rev. Cancer* **2003**, *3*, 243.
- (2) Lewis-Williams, J. D. *Nat. Mater.* **2014**, *13*, 99.
- (3) Baker, M. *Nature* **2010**, *463*, 977.
- (4) Cormode, D. P.; Jarzyna, P. A.; Mulder, W. J. M.; Fayad, Z. A. *Adv. Drug Delivery Rev.* **2010**, *62*, 329.
- (5) Kobayashi, H.; Ogawa, M.; Alford, R.; Choyke, P. L.; Urano, Y. *Chem. Rev.* **2010**, *110*, 2620.
- (6) Smith, A. M.; Mancini, M. C.; Nie, S. *Nat. Nanotechnol.* **2009**, *4*, 710.
- (7) Birks, J. B. *Photophysics of Aromatic Molecules*; Wiley: London, 1970.
- (8) Mei, J.; Leung, N. L. C.; Kwok, R. T. K.; Lam, J. W. Y.; Tang, B. Z. *Chem. Rev.* **2015**, *115*, 11718.
- (9) Ma, N.; Sargent, E. H.; Kelley, S. O. *Nat. Nanotechnol.* **2009**, *4*, 121.
- (10) Wei, W.; He, X.; Ma, N. *Angew. Chem., Int. Ed.* **2014**, *53*, 5573.
- (11) Xiong, L.-H.; Cui, R.; Zhang, Z.-L.; Yu, X.; Xie, Z.; Shi, Y.-B.; Pang, D.-W. *ACS Nano* **2014**, *8*, 5116.
- (12) Zhou, B.; Shi, B.; Jin, D.; Liu, X. *Nat. Nanotechnol.* **2015**, *10*, 924.
- (13) Yong, K.-T.; Law, W.-C.; Hu, R.; Ye, L.; Liu, L.; Swihart, M. T.; Prasad, P. N. *Chem. Soc. Rev.* **2013**, *42*, 1236.
- (14) Gnach, A.; Lipinski, T.; Bednarkiewicz, A.; Rybka, J.; Capobianco, J. A. *Chem. Soc. Rev.* **2015**, *44*, 1561.
- (15) Lee, K.; Cui, Y.; Lee, L. P.; Irudayaraj, J. *Nat. Nanotechnol.* **2014**, *9*, 474.
- (16) Liu, Y.; Huang, C. Z. *ACS Nano* **2013**, *7*, 11026.
- (17) Gao, P. F.; Gao, M. X.; Zou, H. Y.; Li, R. S.; Li, Y. F.; Huang, C. Z. *Chem. Sci.* **2016**, *7*, 5477.
- (18) Anker, J. N.; Hall, W. P.; Lyandres, O.; Shah, N. C.; Zhao, J.; Van Duyne, R. P. *Nat. Mater.* **2008**, *7*, 442.
- (19) Lusic, H.; Grinstaff, M. W. *Chem. Rev.* **2013**, *113*, 1641.
- (20) Yu, S.-B.; Watson, A. D. *Chem. Rev.* **1999**, *99*, 2353.
- (21) Dulkeith, E.; Ringler, M.; Klar, T. A.; Feldmann, J.; Muñoz Javier, A.; Parak, W. J. *Nano Lett.* **2005**, *5*, 585.
- (22) Schreiber, R.; Do, J.; Roller, E.-M.; Zhang, T.; Schüller, V. J.; Nickels, P. C.; Feldmann, J.; Liedl, T. *Nat. Nanotechnol.* **2014**, *9*, 74.
- (23) He, X.; Zeng, T.; Li, Z.; Wang, G.; Ma, N. *Angew. Chem., Int. Ed.* **2016**, *55*, 3073.
- (24) Luo, X.; Li, Z.; Wang, G.; He, X.; Shen, X.; Sun, Q.; Wang, L.; Yue, R.; Ma, N. *ACS Appl. Mater. Interfaces* **2017**, *9*, 33624.
- (25) Jin, Y.; Gao, X. *Nat. Nanotechnol.* **2009**, *4*, 571.
- (26) Ji, B.; Giovanelli, E.; Habert, B.; Spinicelli, P.; Nasilowski, M.; Xu, X.; Lequeux, N.; Hugonin, J.-P.; Marquier, F.; Greffet, J.-J.; Dubertret, B. *Nat. Nanotechnol.* **2015**, *10*, 170.
- (27) Luo, W.; Wu, M.; Li, S.; Xu, Y.; Ye, Z.; Wei, L.; Chen, B.; Xu, Q.-H.; Xiao, L. *Anal. Chem.* **2016**, *88*, 6827.
- (28) Luo, J.; Xie, Z.; Lam, J. W. Y.; Cheng, L.; Chen, H.; Qiu, C.; Kwok, H. S.; Zhan, X.; Liu, Y.; Zhu, D. *Chem. Commun.* **2001**, 1740.
- (29) Mei, J.; Hong, Y.; Lam, J. W. Y.; Qin, A.; Tang, Y.; Tang, B. Z. *Adv. Mater.* **2014**, *26*, 5429.
- (30) Liang, J.; Tang, B. Z.; Liu, B. *Chem. Soc. Rev.* **2015**, *44*, 2798.
- (31) Hu, Q.; Gao, M.; Feng, G.; Liu, B. *Angew. Chem., Int. Ed.* **2014**, *53*, 14225.
- (32) Yuan, Y.; Zhang, C.-J.; Gao, M.; Zhang, R.; Tang, B. Z.; Liu, B. *Angew. Chem., Int. Ed.* **2015**, *54*, 1780.
- (33) Hong, Y.; Lam, J. W. Y.; Tang, B. Z. *Chem. Soc. Rev.* **2011**, *40*, 5361.
- (34) Kwok, R. T. K.; Leung, C. W. T.; Lam, J. W. Y.; Tang, B. Z. *Chem. Soc. Rev.* **2015**, *44*, 4228.
- (35) Ding, D.; Li, K.; Liu, B.; Tang, B. Z. *Acc. Chem. Res.* **2013**, *46*, 2441.
- (36) Shi, H.; Kwok, R. T. K.; Liu, J.; Xing, B.; Tang, B. Z.; Liu, B. J. *Am. Chem. Soc.* **2012**, *134*, 17972.
- (37) Hong, Y.; Meng, L.; Chen, S.; Leung, C. W. T.; Da, L.-T.; Faisal, M.; Silva, D.-A.; Liu, J.; Lam, J. W. Y.; Huang, X.; Tang, B. Z. *J. Am. Chem. Soc.* **2012**, *134*, 1680.
- (38) Leung, C. W. T.; Hong, Y.; Chen, S.; Zhao, E.; Lam, J. W. Y.; Tang, B. Z. *J. Am. Chem. Soc.* **2013**, *135*, 62.
- (39) Gui, C.; Zhao, E.; Kwok, R. T. K.; Leung, A. C. S.; Lam, J. W. Y.; Jiang, M.; Deng, H.; Cai, Y.; Zhang, W.; Su, H.; Tang, B. Z. *Chem. Sci.* **2017**, *8*, 1822.
- (40) Yuan, Y.; Xu, S.; Cheng, X.; Cai, X.; Liu, B. *Angew. Chem., Int. Ed.* **2016**, *55*, 6457.
- (41) Yuan, Y.; Liu, B. *Chem. Sci.* **2017**, *8*, 2537.
- (42) Wang, Y.; Chen, M.; Alifu, N.; Li, S.; Qin, W.; Qin, A.; Tang, B. Z.; Qian, J. *ACS Nano* **2017**, *11*, 10452.
- (43) Gu, B.; Wu, W.; Xu, G.; Feng, G.; Yin, F.; Chong, P. H. J.; Qu, J.; Yong, K.-T.; Liu, B. *Adv. Mater.* **2017**, *29*, 1701076.
- (44) Yuan, Y.; Kwok, R. T. K.; Tang, B. Z.; Liu, B. *J. Am. Chem. Soc.* **2014**, *136*, 2546.
- (45) Chen, S.; Hong, Y.; Liu, Y.; Liu, J.; Leung, C. W. T.; Li, M.; Kwok, R. T. K.; Zhao, E.; Lam, J. W. Y.; Yu, Y.; Tang, B. Z. *J. Am. Chem. Soc.* **2013**, *135*, 4926.
- (46) Chan, J.; Dodani, S. C.; Chang, C. J. *Nat. Chem.* **2012**, *4*, 973.
- (47) Liu, Y.; Tang, Y.; Barashkov, N. N.; Irgibaeva, I. S.; Lam, J. W. Y.; Hu, R.; Birimzhanova, D.; Yu, Y.; Tang, B. Z. *J. Am. Chem. Soc.* **2010**, *132*, 13951.
- (48) Xie, J.; Lee, J. Y.; Wang, D. I. C.; Tin, Y. P. *ACS Nano* **2007**, *1*, 429.
- (49) Love, S. A.; Maurer-Jones, M. A.; Thompson, J. W.; Lin, Y.-S.; Haynes, C. L. *Annu. Rev. Anal. Chem.* **2012**, *5*, 181.
- (50) Zou, Y.; Wei, Y.; Wang, G.; Meng, F.; Gao, M.; Storm, G.; Zhong, Z. *Adv. Mater.* **2017**, *29*, 1603997.
- (51) Hu, F.; Huang, Y.; Zhang, G.; Zhao, R.; Yang, H.; Zhang, D. *Anal. Chem.* **2014**, *86*, 7987.